Tsunami Hazard in the South–East Aegean Sea

D.A. Mitsoudis[a,b], E.T. Flouri[a,c], N. Chrysoulakis[a], Y. Kamarianakis[a,d], E.A. Okal[e], C.E. Synolakis[c,f,g]

[a] *Institute of Applied and Computational Mathematics, FORTH, GR-70013 Heraklion, Crete, Greece.*
[b] *Department of Applied Mathematics, University of Crete, GR-71409 Heraklion, Greece.*
[c] *Department of Environmental Engineering, Technical University of Crete, GR-73100 Chania, Greece.*
[d] *School of Civil & Environmental Engineering, Cornell University, Ithaca, USA.*
[e] *Department of Earth and Planetary Sciences, Northwestern University, Evanston, IL 60208, USA.*
[f] *Hellenic Center for Marine Research, Anavyssos, Attica, Greece.*
[g] *Department of Civil Engineering, University of Southern California, Los Angeles, CA 90089, USA.*

Abstract

We present a systematic assessment of the earthquake-generated tsunami hazard for the Greek island of Rhodes in the SE Aegean Sea. Our approach is based on numerical hydrodynamic simulations, including inundation computations, with MOST, coupled with accurate bathymetry and topography data of the study area. We have considered several hypothetical, credible, near-field 'worst case' scenarios, and, here we present results for four, associated with seismic events of magnitude 8.0 to 8.4. Our results include calculations of the maximum inundation, the maximum wave elevation and the maximum flow depth in specific locales, and assess the influence of the epicenter location on the tsunami hazard, for time windows of 100, 500 and 1000 years. We illustrate our findings with lines superimposed on satellite images, as maps indicating the estimated maximum values, and in terms of two-dimensional histograms. Given that our composite inundation for a 1000 year time period with our Monte Carlo variation of epicenters is overall larger than the inundation computed for existing well-established 'worst case' scenarios, we caution the indiscriminate use of the latter in evaluating inundation in highly populated areas.

Keywords: tsunamis; runup; numerical simulations; inundation maps; seismic hazard; Aegean Sea; Rhodes;

1. Introduction

The Aegean Sea features one of the most active and complicated seismotectonic structures worldwide. The Greek and Turkish coastlines have been populated for thousands of years and have experienced several tsunamis, some of them having been characterized as devastating. While one might argue that the occurrence of tsunamis is rare in the Aegean Sea, especially compared to the Pacific or Indian Oceans, nevertheless, the hazard needs to be evaluated, since many of the Aegean coastal areas are densely populated, and have undergone rapid economic development during the last decades. Given the overall lack of public awareness about evacuations, even marginal events may have significant impact.

The efforts in determining tsunami hazard for Greece and adjacent coastal areas date back several decades. Up until about 2000 most efforts were concentrated in the collection of historical data and in the compilation and analysis of tsunami catalogs (Galanopoulos, 1960; Ambraseys, 1962; Papadopoulos and Chalkis, 1984; Papazachos et

al., 1986; Soloviev, 1990; Papazachos and Dimitriu, 1991; Altınok and Ersoy, 2000). Since then, and especially after the 2004 Indian Ocean tsunami, there was more scientific interest focused in the broader Mediterranean region and consequently in the Aegean Sea, resulting in versatile ways of assessing tsunami hazard. These include numerical simulations based on scenarios of the activation of potential sources (Tinti et al., 2005; Tselentis et al., 2010); the use of geological records of tsunamis (Dominey-Howes, 2002); updated tsunami catalogs along with empirical probabilistic hazard assessment (Papadopoulos et al., 2007); and the use of modern seismological techniques integrating surveyed run-up values with results from numerical simulations that employ run-up calculations, as was done recently for the 1956 Amorgos earthquake by Okal et al. (2009). Further, European projects such as TRANSFER (http://www.transferproject.eu/) – an FP6 project with 30 partners from 12 different countries – have helped better understand tsunami hazards in the Mediterranean.

The present work aims at a systematic assessment of the earthquake-generated tsunami hazard in the SE Aegean Sea, particularly for the island of Rhodes (*Ρόδος*), located between latitudes 35.85°N and 36.5°N and longitudes 27.6°E and 28.3°E, opposite Asia Minor. Rhodes is the largest and most populated island in the SE Aegean, and has been hit by severe earthquakes, such as the events of 227 BC, and AD 1303, 1481 and 1851, which were related, with variable degrees of confidence, to the occurrence of tsunamis (Ambraseys, 2009). We note that Ambraseys and Synolakis (2010) have argued that without both geologic and sedimentologic evidence corroborating historic reports, the occurrence of any historic tsunami should be considered tentative. Nowadays, the potential impact due to an extreme event is likely to be much greater, since a larger population is concentrated in coastal areas, and there is much greater economic and touristic activity and infrastructure. We also note that with the exception of Okal et al. (2009) and Flouri et al. (2011), existing studies of tsunami impact in the Aegean or the Ionian Seas have not performed inundation computations. Rather, they present offshore propagation results, and, on occasion, employ empirical one dimensional formulae to relate offshore wave heights with onshore run-up.

To assess the tsunami hazard for Rhodes, we use efficient numerical modeling coupled with updated and highly accurate bathymetry and topography data. In the next section, we briefly present the numerical model used to perform the tsunami simulations and the necessary bathymetry and topography data. In Section 3, we present deterministic inundation maps for Rhodes, based on "worst" case scenarios intended to assess the impact of hypothetical, particularly large, seismic events. Section 4 introduces the probabilistic framework and the methodology used to produce probabilistic maps in this case, based on multiple tsunami scenarios, and aims at quantifying inherent uncertainties, which stem mostly from the geographic distribution of seismic sources. We then discuss the outcome of our computations which suggest that our 1000–year probabilistic analysis produces results which feature more extensive inundation than widely accepted "worst case" scenario simulations.

2. The tsunami simulation method

The study of the evolution of earthquake-generated tsunami waves is usually separated into three distinctive stages: generation, propagation, and runup. In this study we perform the simulation of the evolution of a tsunami wave with MOST (Method of Splitting Tsunamis), a numerical model developed by Titov and Synolakis (1998). MOST has been extensively validated through comparisons with benchmark experiments and field data and has been proven effective in computing all three stages, thus providing a complete tsunami simulation capability (Yeh et al., 1996; Liu et al., 2008; Synolakis et al., 2008).

We briefly present here the basic features of MOST. In the deformation phase, an initial condition for the hydrodynamic computation is derived by calculating the ocean floor deformation due to a seismic event (Gusiakov, 1978; Okada, 1985). The elastic fault plane model is implemented with the aid of a formula for static sea-floor deformation (Titov, 1997), and initial conditions are calculated for the subsequent phase of tsunami propagation and inundation. In the propagation phase, the Nonlinear Shallow Water (NSW) wave equations are solved numerically using a split-step characteristics-finite difference scheme, similar to that described in Titov (1997). Here the tsunami evolution is across the open sea. Finally, in the inundation phase, coastal flooding and inundation are simulated by extending the propagation calculations with the aid of a multi-grid runup algorithm (Titov and Synolakis, 1998). In order to perform simulations with MOST, the following sets of input data are required, one, detailed information on seismic source mechanisms for the computation of the sea-floor dislocation induced by the seismic event, two, gridded bathymetric data information for the open sea propagation, and, three, a set of gridded Digital Elevation Models (DEM) containing bathymetry and topography for use during the inundation phase.

Here, the main data sources used for the bathymetry-topography reconstruction were bathymetry/topography data of 1 min resolution from GEBCO (General Bathymetric Chart of the Oceans) of the British Oceanographic Data Centre, nautical charts of various scales and resolutions, bathymetry binary data extracted from ENC's (Electronic Nautical Charts), and shoreline data purchased from the Hellenic Navy Hydrographic Service. In addition, ASTER 15 m pixel satellite images for the island of Rhodes from the NASA EOS Data Center, an Ikonos 1 m satellite image covering the NE part and a Digital Terrain Model (DTM) for the Municipality of Rhodes produced by photogrammetric analysis of stereo aerial images of high resolution (x, y: 5 m, $z < 1$ m). Finally, Global Positioning System (GPS) data from field measurements have been used for the registration of the above data sets.

These data were checked and orthorectified, where appropriate, according to a common and consistent georeference. Remote sensing techniques have been used for the orthorectification of the satellite images, and for the construction of accurate DEM's (Chrysoulakis et al., 2008, 2011). Subsequently, the resulting data were uploaded on a GIS using the ArcGIS v. 9.0 platform of ESRI. During the coupling of the bathymetry and topography dataset to the GIS, significant discrepancies occurred in the definition of the shoreline. For this purpose, up-to-date feature extraction techniques (see Lipakis et al., 2008 and the references therein) have been used for the definition of a new, accurate shoreline dataset from the Ikonos image. Using this accurate shoreline dataset, the topographic and bathy-

metric grids were merged into the final Digital Elevation Model (DEM), from which three raster ASCII nested grid files were extracted.

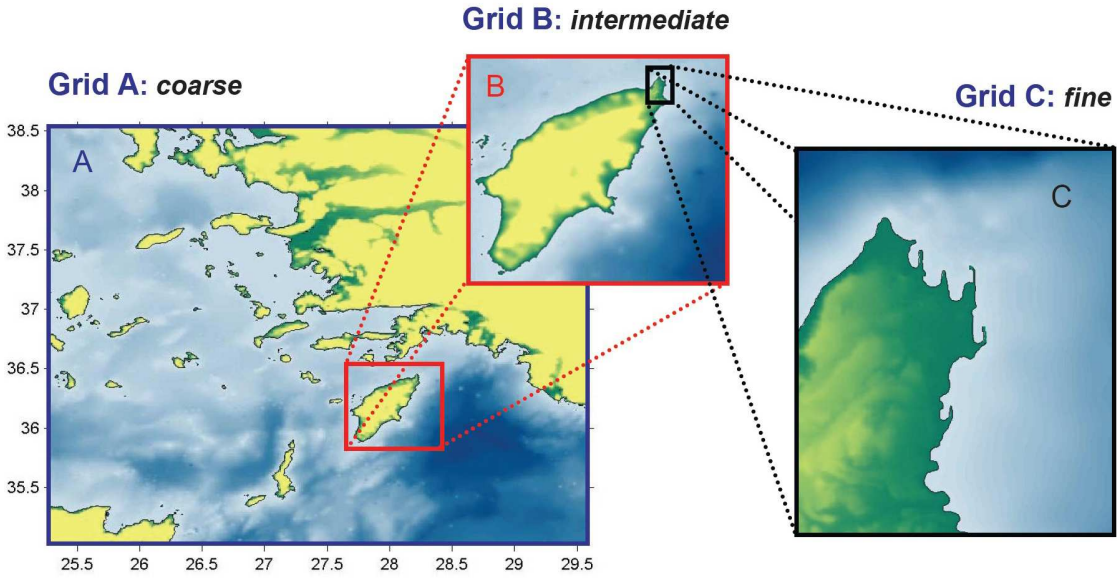

Figure 1: A map of the SE Aegean Sea. Geographic location of the three nested computational grids for Rhodes. Grid C is used for inundation computations.

Grid A	coarse	$\Delta x = \Delta y = 0.01^\circ$ (~ 1113 m)	697×498 nodes
Grid B	intermediate	$\Delta x = \Delta y = 0.00166^\circ$ (~ 185 m)	401×451 nodes
Grid C	fine	$\Delta x = \Delta y = 0.00027^\circ$ (~ 30 m)	288×252 nodes

Table 1: Spatial resolution of bathymetry-topography grids used in this study.

As previously mentioned, MOST requires a set of gridded DEM's containing bathymetry and topography for use during the inundation phase. In the case of Rhodes, three nested grids were used (referred to as A, B, C from coarsest to finest), whose location and parameters are given in Fig. 1 and Table 1. We emphasize that the development of the computational grids for Rhodes was an essential and non-trivial part of this study. The resolution of the finest grid (~ 30 m sampling) is likely adequate to capture the inundation characteristics of large waves, such as those expected from extreme events. A similar resolution has been used in the production of inundation maps of California by (Uslu et al., 2007; Barberopoulou et al., 2011). In all our computations, the time step was taken equal to 0.3 s; for this value the CFL condition (Courant et al., 1928) was satisfied.

3. Tsunami simulations based on “worst case” scenarios

It is quite common for assessing the tsunami hazard in a particular region to run numerical simulations corresponding to large events known from existing tsunami catalogs or inferred from geological investigations (Legg et al., 2004; Okal et al., 2003). For the area of Rhodes, historic reports are interpreted in the most recent work of Ambraseys (2009). The events of AD 142, 1303, 1481 and possibly 1851 are cited with variable reliability. On the other hand, very few large tsunamis due to submarine earthquakes have occurred in the Mediterranean since the birth of instrumental seismology, and none of them seem to have had considerable impact on Rhodes. As a consequence, the task of relating historic tsunamis with reliable earthquake data is not free of ambiguities, leading to uncertainties on the epicentral location of the parent earthquake, and thus discrepancies in the estimates from different studies.

We have experimented with various ‘extreme’ scenarios associated with seismic events of magnitude approximately 8.0 or larger. Such earthquakes have been inferred along the Hellenic Arc (Shaw et al., 2008). Here, we present the outcome of four possible near-field scenarios, hereafter labeled S1–S4, whose source parameters are given in Table 2. In Fig. 2, we illustrate the position and shape of the associated initial conditions (wave elevation). Next, we describe the rationale behind our selections.

Scenario	S1	S2	S3	S4
Magnitude M_w	8.4	8.1	8.1	8.0
Longitude (deg)	28.4	28.4	28.4	29
Latitude (deg)	35.5	35.5	35.5	36.1
Length (km)	190	190	140	150
Width (km)	90	35	70	35
Dip (deg)	20	20	20	20
Rake (deg)	90	90	90	90
Strike (deg)	235	300	235	300
Slip (m)	5	5	4	5
Depth (km)	7.5	1	10	5

Table 2: Seismic parameters of four selected “worst case” scenarios. (The depth is the closest distance from the fault plane to the seafloor or ground surface.) Scenario S2 is directly from Tinti et al. (2005).

The parameters for Scenarios S1 and S3 were obtained empirically by using the available bathymetry and information on local tectonics to position the two events at the contact of the inferred subducting block Southeast of Rhodes; S1 considers a 190 km long fault, while S3 features a shorter rupture of only 140 km. Scaling laws (Geller, 1976) were used to obtain the width and seismic slips of the events, whose combination yields a seismic moment, expressed in Table 2 as an equivalent magnitude (Kanamori, 1977). The parameters of Scenario S2 were taken from Tinti et al.

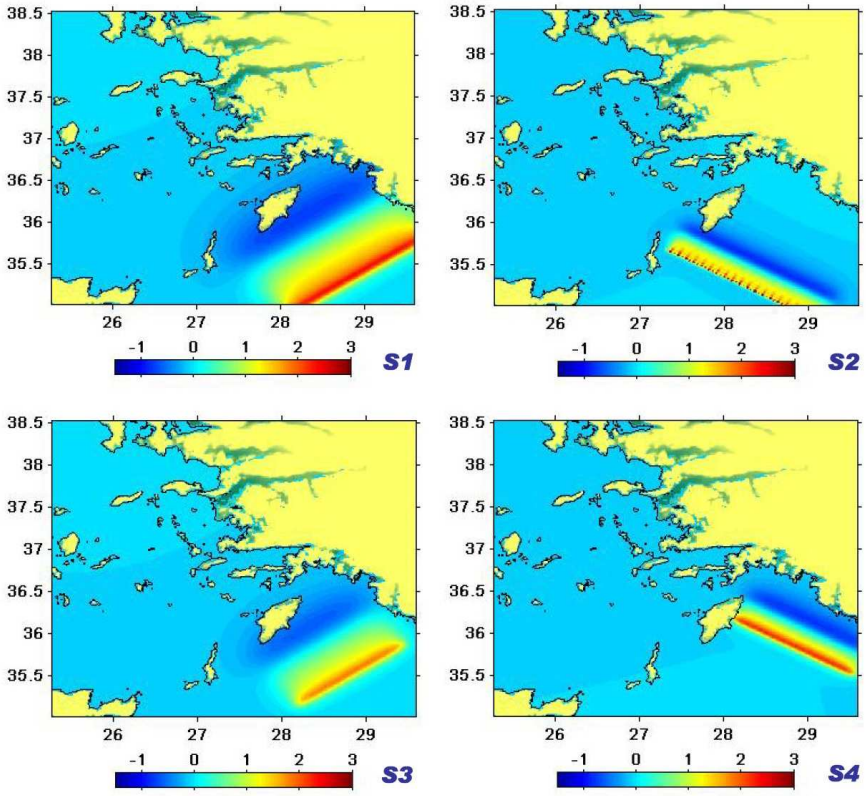

Figure 2: Initial conditions (wave elevation) for the four extreme scenarios S1–S4. S2 and S4 are scenarios from Tinti et al. (2005) and Papazachos (1996).

(2005). Those of S4 combine, for the large earthquake of AD 1303, Tinti *et al.*'s (2005) values of strike, dip, rake and seismic slip with Papazachos' (1996) location estimate.

Next, we present our results that provide estimates of the inundated area and of the *maximum wave elevation*, $\eta_{\max} = \max_t \eta(x, y; t)$, at each grid point, for each of the four scenarios, where $\eta(x, y; t)$ denotes the elevation of the water above the undisturbed mean sea level at each point (x, y) and at time t. We also compute the *maximum flow depth*, $h_{\max}(x, y) = \max_t h(x, y; t)$, defined as the maximum over t of the flow depth $h(x, y; t) = \eta(x, y; t) + d(x, y)$, where $d(x, y)$ denotes the function determining the bathymetry and topography data with respect to an undisturbed mean sea level ($d(x, y) > 0$ at sea and $d(x, y) < 0$ on land). In all cases, the maximum is calculated over the total temporal interval, *i.e.* from time $t = 0$ until the end of the computation, simulating about 45 min of wave evolution. We have checked (see the discussion following Fig. 4 below) that this time window suffices to capture the maximum values of the examined parameters.

In Fig. 3 we plot the estimated inundated area due to the four scenarios. S1 seems to have the worst impact in terms of the inundated area, although in most areas the four lines do not differ significantly. The commercial harbour,

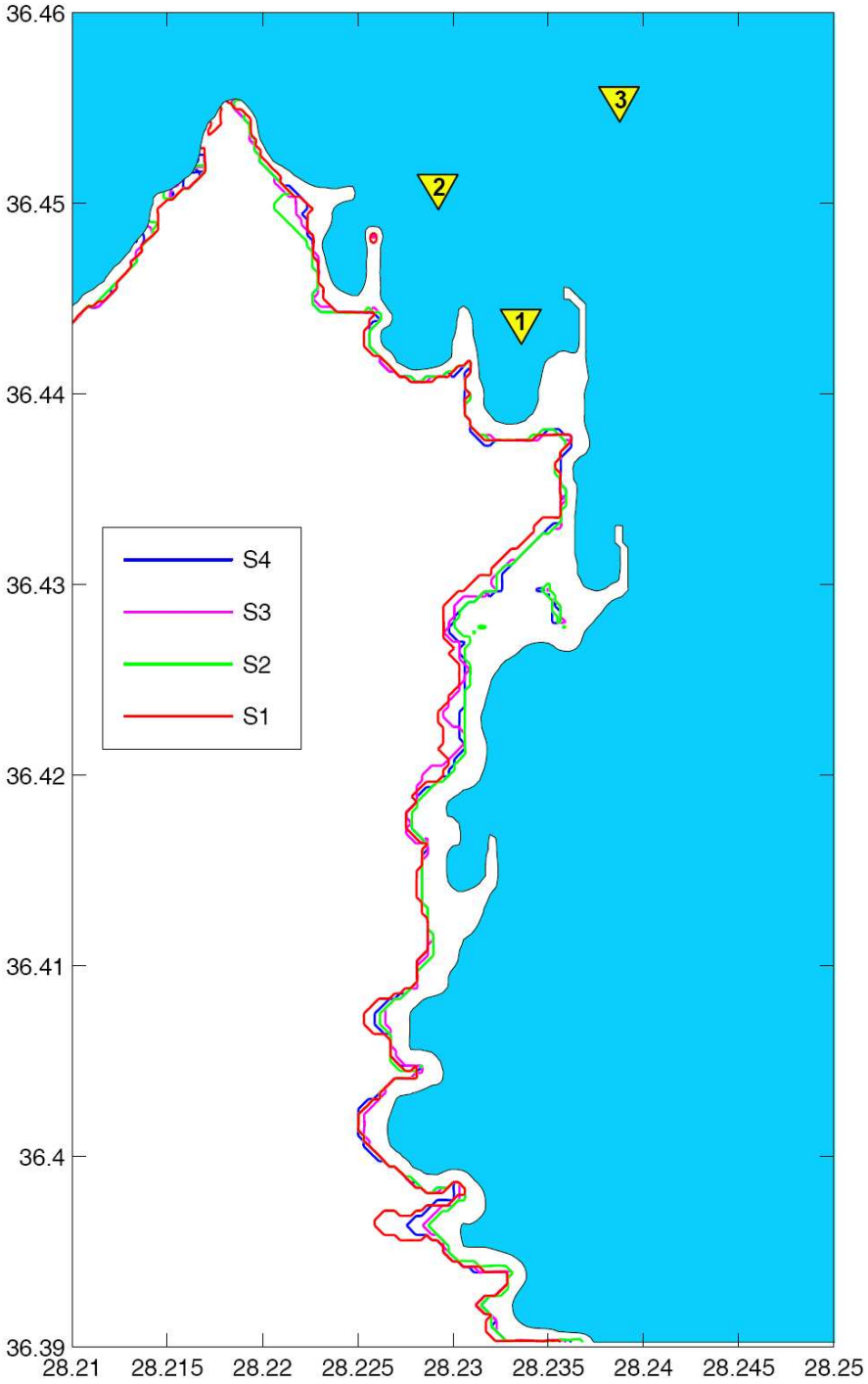

Figure 3: Inundation lines for the four 'worst' scenarios. The yellow triangles mark the location of wave gauges, whose recordings for Scenarios S1 and S4 are shown in Fig. 4.

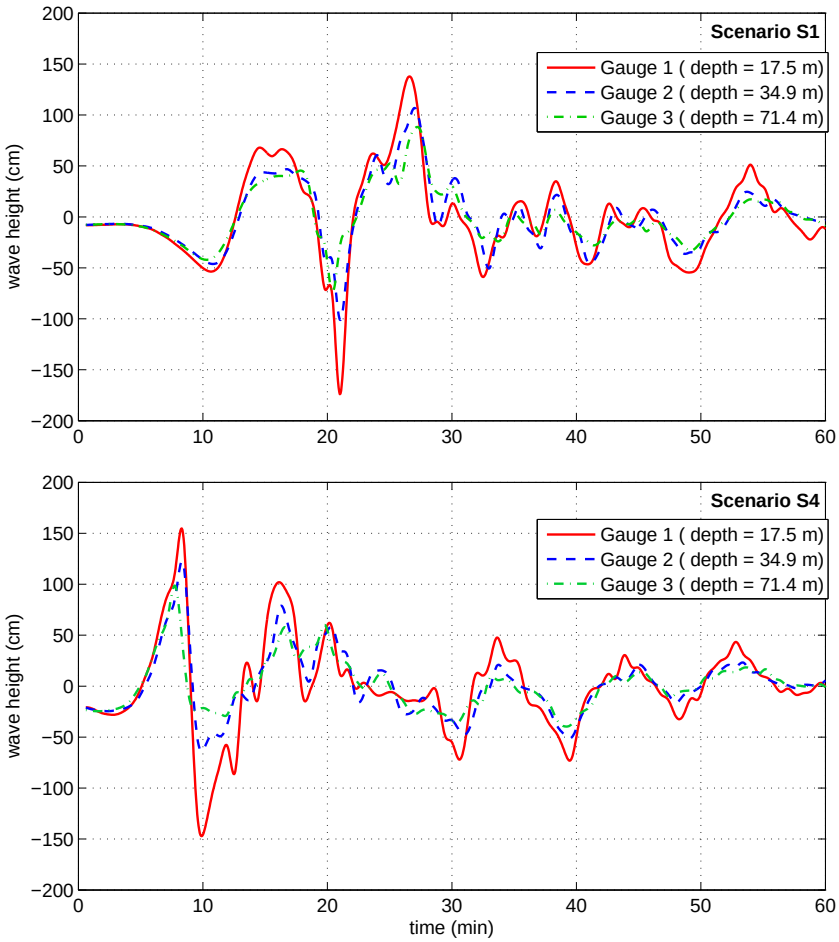

Figure 4: Computed time series of wave elevation at three virtual wave gauges for Scenarios S1 (top) and S4 (bottom). The location of the wave gauges is marked with yellow triangles in Fig. 3.

the beaches located at the northern tip of the island, and the eastern part of the city, where the popular Zefyros beach and the city cemetery are located, seem to be affected by tsunamis from all scenarios.

In Fig. 4 we plot the computed wave elevation versus time for Scenarios S1 and S4 at three virtual wave gauges, their location is marked with yellow triangles in Fig. 3. Note that the results depicted in this figure were obtained by extending our computations to simulate 1 h of wave propagation and indicate that 45 min suffices to observe the maximum values. The two tsunamis manifest themselves immediately with a withdrawal of the water surface due to subsidence, *i.e.* as leading depression N waves (Tadepalli and Synolakis, 1994). The maximum value of the wave elevation in S1 reaches $\sim$ 1.4 m, and is exhibited from the second wave in Gauge 1, located inside the commercial harbour. In S4 the maximum value slightly exceeds 1.5 m in the first wave, also in Gauge 1. (The behaviour of S2 is similar to S1, and S3 resembles S1, so we do not present them here.)

Figure 5 summarizes the results for the maximum elevation of the wave $\eta_{\max}(x, y)$, for the four scenarios. Addi-

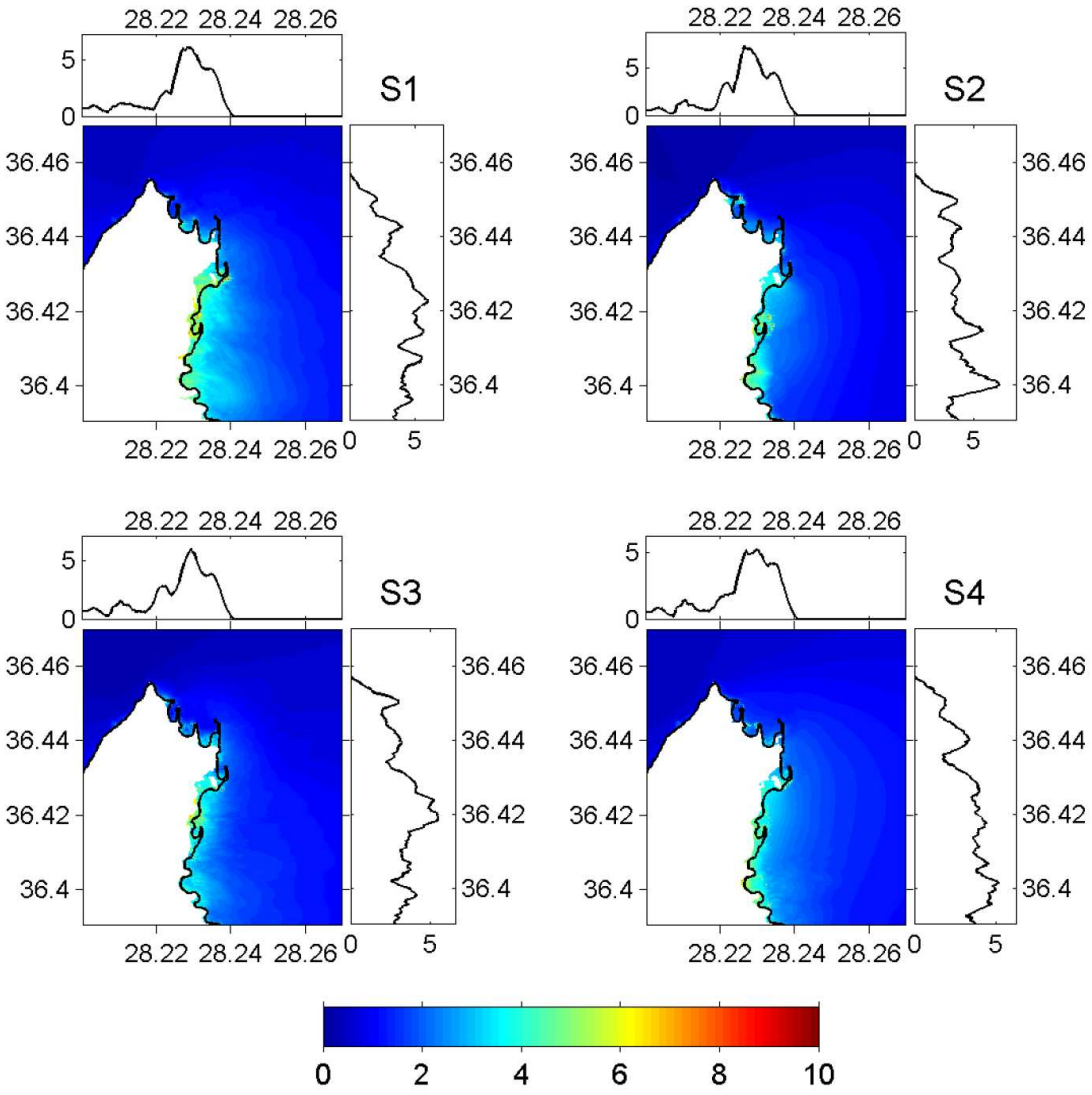

Figure 5: Maximum wave elevation $\eta_{\max}$ in meters and elevation of the inundation limits for Scenarios S1-S4, of Table 2.

tionally, the elevation of the inundation line is illustrated in separate horizontal and vertical subplots for the x and y coordinates, respectively. All the results are in meters and indicate that, in Scenario S1, the elevation of the inundation line exceeds 5 m several times. In S4, it reaches and remains a little below 5 m for most of the eastern coastal area, while the overall highest run-up value, ~7 m, is observed in Scenario S2. In Fig. 6, we plot the values of the maximum flow depth $h_{\max}(x, y)$ for the four scenarios. The value $h_{\max}(x, y)$ has been calculated for all the grid points inland, and all the results are in meters. Again, these results identify S1 as the worst scenario. The most vulnerable area, in the sense of a maximum flow depth of between 2 and 5 m, appears concentrated along the eastern coastal area, between latitudes 36.40°N and 36.43°N.

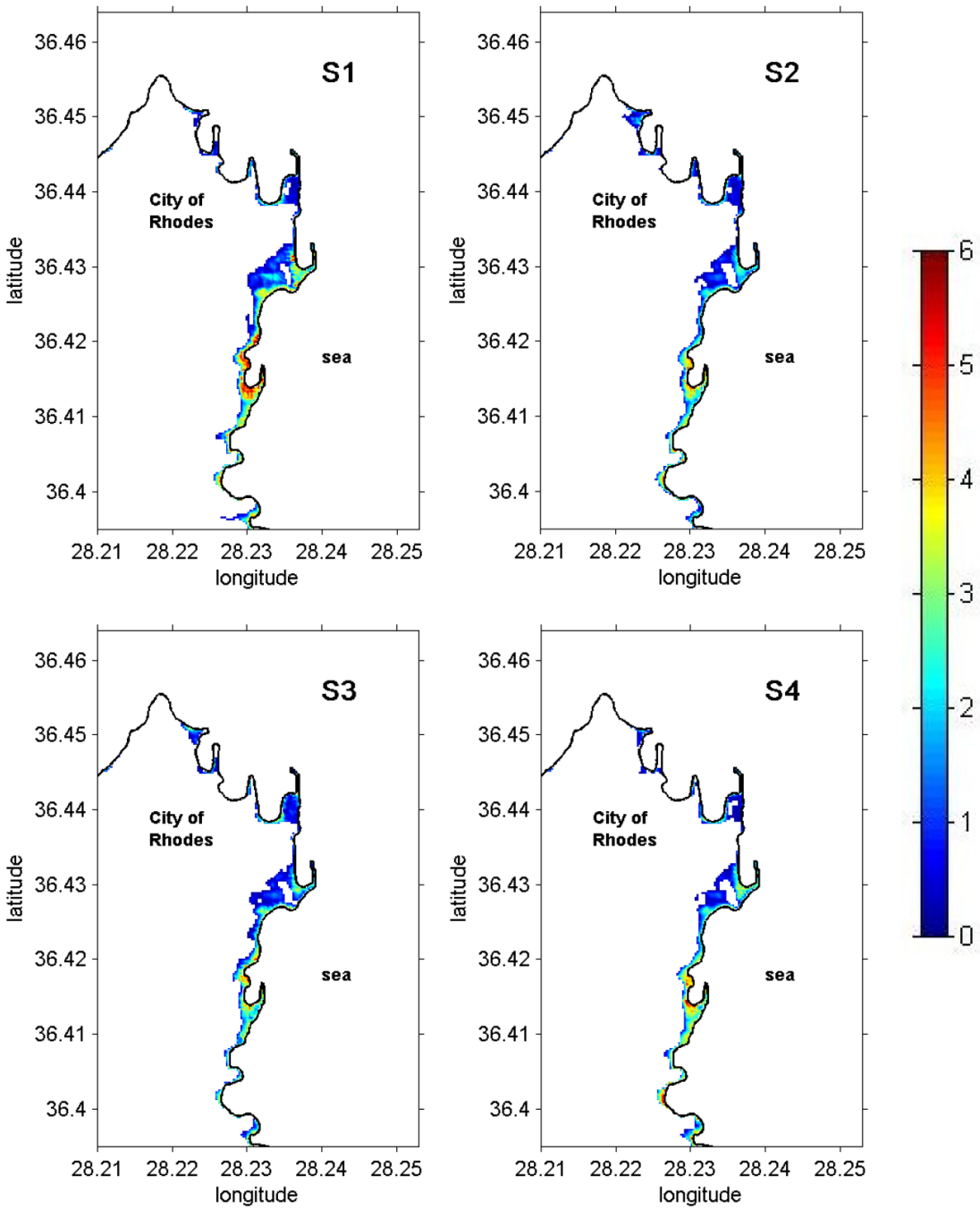

Figure 6: Maximum flow depth h_{max} in meters for Scenarios S1-S4, of Table 2.

4. Tsunami simulations based on a probabilistic approach

In this section, we present a different approach for assessing the tsunami risk for the area under consideration. In general, Probabilistic Tsunami Hazard Assessment (PTHA) is an alternative to the worst case scenarios approach for estimating tsunami potential and impact for site-specific studies. When there are sufficient data catalogs, such as observed wave heights, one may empirically analyze them and derive hazard curves. Otherwise, and in the absence of geographic inference about slip rates, the use of computational methods becomes necessary.

Most of the established methodologies for PTHA follow the lines of the well established Probabilistic Seismic Hazard Analysis (PSHA) (Geist and Parsons, 2006). Following the earthquake analogy, the tsunami problem may be divided into the generation, propagation and run-up phase, and the various uncertainties corresponding to each phase should be identified. The phase that mostly contributes to uncertainty in a PTHA is usually the generation phase. For example, even when the location of a potentially tsunamigenic fault is known with confidence, the maximum event magnitude that it can generate depends on the slip rate and fault parameters such as depth, length, and width. During the propagation phase, uncertainties are primarily introduced due to the lack of detailed bathymetric data, while the run-up phase is mainly affected by the ability of the model to handle detailed topographic data and to estimate accurately 'site' effects (*e.g.* inundation length and height). Another factor that affects the choice of an appropriate method for performing a PTHA is whether one concentrates on studying far- or near-field events. For instance, Annaka et al. (2007) use a logic-tree approach to derive tsunami hazard curves for assessing quantitatively tsunami risk for coastal facilities in Japan, Power et al. (2007) use a Monte-Carlo technique for estimating the tsunami hazard along the coast of New Zealand considering only distant source events generated by South American earthquakes, and Burbidge et al. (2008) present results of a PTHA for Western Australia for tsunamis generated by subduction zone earthquakes. Recently, González et al. (2009) published probabilistic tsunami flooding maps for Seaside, Oregon, as an outcome of a PTHA which provided estimates on the spatial distribution of tsunami amplitudes with 1% and 0.2% annual probability of exceedance, accounting for both near- and far-field seismic sources.

To date, every probabilistic approach has pros and cons, and there is no consensus on whether time dependent or time independent methods are appropriate (Uslu, 2008). For example, as pointed out by Geist and Parsons (2006), the analysis of the uncertainties associated with near-field events may lead to very complicated and extensive logic trees. On the other hand, Monte-Carlo simulations may be very demanding in terms of computation times, and they have been used solely for referring statistics for far-field events. Then, usually, the hydrodynamic simulation is performed numerically just for the propagation phase and it is terminated in a specific water depth contour (usually 10 m or 50 m), where reflecting boundary conditions are imposed. Next, the computed offshore tsunami amplitudes at the pre-selected isobath are used to estimate inland run-up values via empirical relations, (Power et al., 2007; Burbidge et al., 2008). This approach allows, in general, the simulation of a very large amount of potential tsunami sources, since offshore tsunami modeling is rather insensitive to shallow bathymetry (Burbidge et al., 2008). When inundation tsunami calculations are included, the computations become far more complicated, very sensitive to bathymetry and

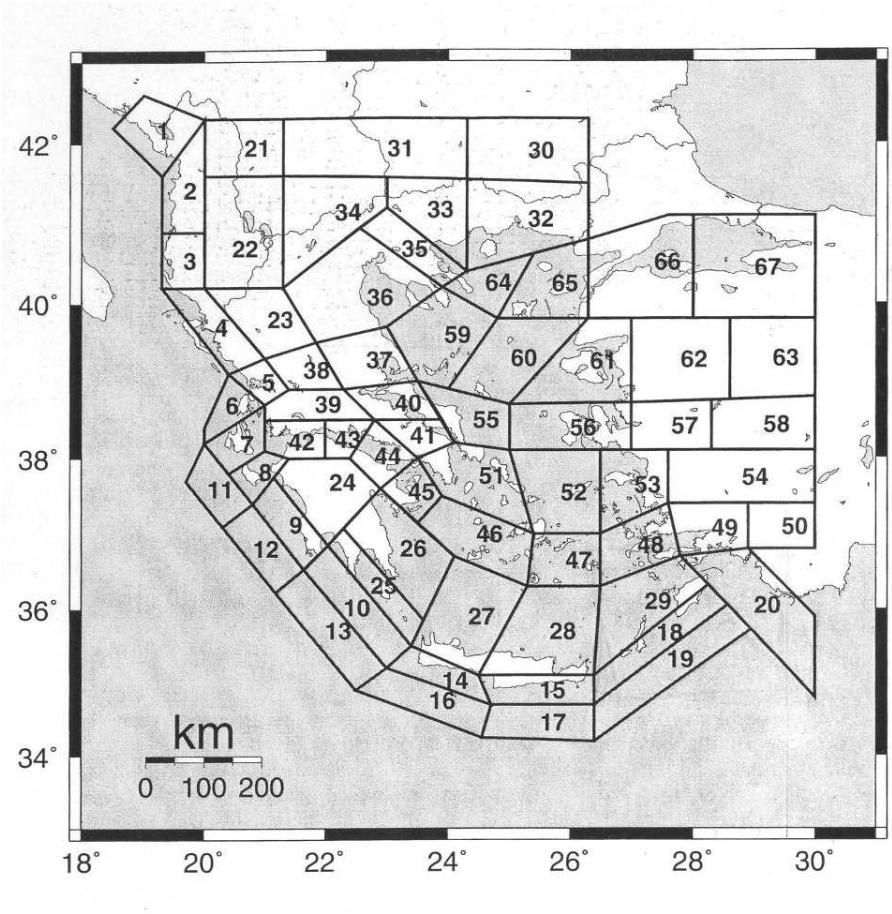

Figure 7: Seismogenic sources of shallow earthquakes in Greece and surrounding areas, after Papazachos and Papazachou (1997).

onshore topography, and very demanding in terms of computation times.

Returning to the case of Rhodes, a search in the existing tsunami catalogs (Ambraseys, 1962; Papadopoulos and Chalkis, 1984; Papazachos et al., 1986; Soloviev, 1990; Papadopoulos et al., 2007; Ambraseys and Synolakis, 2010) reveals that the overwhelming majority of the tsunamis that have been documented to affect Rhodes from antiquity up to now were triggered by strong earthquakes with epicenters distributed all around the offshore area surrounding Rhodes and located, in general, very close to its coasts; see *e.g.* Fig. 3 in Soloviev (1990), Fig. 1 in Altınok and Ersoy (2000) and Fig. 1 in Papadopoulos et al. (2007). Moreover, the number of large tsunamis in this area since the birth of instrumental seismology is probably less than three, and according to Papazachos and Dimitriu (1991), only seismic data since 1962 and thereafter may be considered reliable for Greece. Thus, entries of the seismic source parameters for specific historic events in tsunami catalogs are unverifiable, not to mention that estimated values differ among catalogs. For example, the epicenter of the large event of AD 1303 ($M \sim 8.0$) is placed at 36.3°N, 27.3°E by Papadopoulos and Chalkis (1984) (and repeated in Soloviev's (1990) catalog), but 147 km away at 35.0°N, 27.0°E

by Papadopoulos et al. (2007)'s later repetition, and 154 km away at 36.1°N, 29.0°E by Papazachos (1996). Similar discrepancies accompany entries of the events of AD 1481 and AD 1851.

In this context, we focused on a computationally based method, where the use of a numerical tsunami generation, propagation (and inundation) model helps produce multiple scenarios and derive inundation statistics. Geographic and historical records imply hazard from primarily near-field events, thus the fine structure of bathymetry and topography play a crucial role in estimating tsunami hazard. Hence, in our simulations with MOST, the run-up algorithm is employed in order to estimate damage parameters such as run-up heights or flow depth inland. As already pointed out, in order to include all possible sources of uncertainty one should probably adopt a fully stochastic Monte-Carlo type approach (Spanos and Zeldin, 1998). In this case, the complexity of the study area, and the lack of seismic input, such as the positive identification of potentially tsunamigenic faults, would lead to a considerable increase in the number of the required simulations. (For example, for a coast line ~90 km long, each MOST run simulating 30 min of wave evolution, with a resolution of 30 m in the finest grid, requires 20 min of CPU-time in a dual-core Pentium INTEL XEON 5130 machine with 4 GB RAM running under Linux at 2 GHz FSB 1333 MHz 2×2M).

To keep the set of random source parameters as small as possible, we will try to take full advantage of existing studies about the seismicity of this region. Following Papazachos and Papazachou (1997); Papaioannou and Papazachos (2000); Moratto et al. (2007), Greece and its surrounding region may be divided into 67 hazard zones where shallow seismicity is relatively homogeneous (Fig. 7). Each of these sources is characterized by a representative focal mechanism for which the values of the parameters a and b of the associated Gutenberg-Richter distribution are determined (Papazachos and Papazachou, 1997, Table 7.1, p. 120). Moreover, in a recent work by Moratto et al. (2007), complete representative focal mechanisms (*i.e.* values for strike, dip and rake) were selected for each region (Moratto et al., 2007, Table 1, Fig. 2).

This allows us, as a first approximation, to assess the influence of the epicenter location on the tsunami hazard by treating the location of the earthquake epicenter as random and keeping the rest of the seismic parameters fixed. In what follows, we briefly discuss the mathematical framework of this approach and give details on its application to the specific site.

4.1. Mathematical background

We consider the following problem: Assume that an earthquake occurs in an area denoted by Ω, a bounded subset of $\mathbb{R}^2$, and let the point $\boldsymbol{x}$ in Ω denote the seismic epicenter. Let, $Y(\boldsymbol{x})$ be the maximum flow depth in a given location inland (or, in general, any other damage indicator, not necessarily scalar), i.e. $Y(\boldsymbol{x})$ is the "receiving" function of tsunamis generated at epicenter $\boldsymbol{x}$. Assuming that Y is a random field, so that $Y(\boldsymbol{x}_1), Y(\boldsymbol{x}_2), \ldots$, are independent identically distributed random variables, for any $\boldsymbol{x}_i \in \Omega$, our aim is to estimate statistically the quantity $U = \max Y(\boldsymbol{x})$, for $\boldsymbol{x}$ in Ω. To this end, $Y(\boldsymbol{x})$ may be viewed as a random variable with cumulative distribution function (CDF) $\mathbb{P}\{Y(\boldsymbol{x}) \leq u\} = F_Y(u)$, assumed to be strictly increasing, *i.e.* behaving as in Fig. 8. For each $\boldsymbol{x}_k$, $k = 1, \ldots, N$, we run MOST for an appropriate earthquake size, which we will discuss below, and compute $Y(\boldsymbol{x}_k)$. Then, we estimate

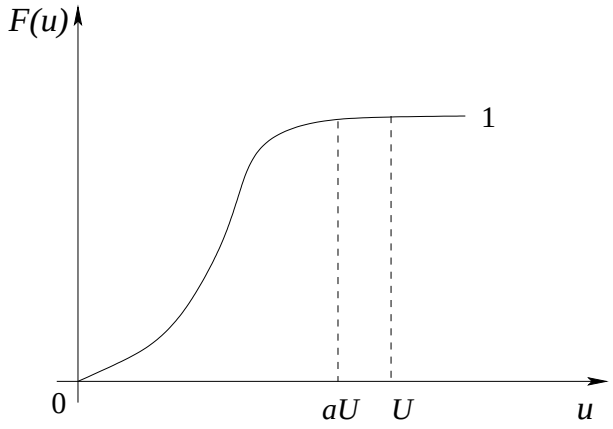

Figure 8: Schematic representation of the CDF of the random variable $Y(\boldsymbol{x})$. ($Y(\boldsymbol{x})$ is the "receiving" function for waves generated at epicenter $\boldsymbol{x}$.)

U by the quantity $\widehat{U}_N = \max\{Y(\boldsymbol{x}_1), Y(\boldsymbol{x}_2), \ldots, Y(\boldsymbol{x}_N)\}$. Under the above assumptions, it is easy to show that $\widehat{U}_N$ will converge to U, as N grows, in a certain sense, *i.e.* $\widehat{U}_N \to U$ in probability (Shiryaev, 1996).

Indeed, let us consider a constant $0 < \alpha < 1$. Then, (Shiryaev, 1996)

$$\mathbb{P}\Big[\widehat{U}_N \le \alpha U\Big] = \mathbb{P}\Big[\max_{1\le k\le N} Y(\boldsymbol{x}_k) \le \alpha U\Big] = \mathbb{P}\Big[\bigcap_{k=1}^{N}\{Y(\boldsymbol{x}_k) \le \alpha U\}\Big] = F_Y(\alpha U)^N.$$

By the definition of U and since $0 < \alpha < 1$, we conclude that $F_Y(\alpha U) < 1$ and, therefore, $\mathbb{P}\Big[\widehat{U}_N \le \alpha U\Big] \longrightarrow 0$ which implies that $\widehat{U}_N \to U$ in probability.

Moreover, if the rate of convergence is fast enough, then $\sum_N F_Y(\alpha U)^N < +\infty$, and the Borel-Cantelli Lemma, (Shiryaev, 1996), assures that $\widehat{U}_N \to U$ almost surely, *i.e.* $\widehat{U}_N$ will be a *consistent estimator* of U. Of course, we do not know $F_Y(\alpha U)$ analytically, but one may try to estimate it as follows: The law of large numbers implies that

$$\lim_{N\to\infty} \frac{\sharp\{k \le N : Y(\boldsymbol{x}_k) \le \alpha U\}}{N} = \mathbb{P}\Big[Y(\boldsymbol{x}) \le \alpha U\Big] = F_Y(\alpha U),$$

therefore $F_Y(\alpha U)$ may be estimated by the quantity $\dfrac{\sharp\{k \le N : Y(\boldsymbol{x}_k) \le \alpha \widehat{U}_N\}}{N}$ known as a histogram. (The notation $\sharp\{\cdot\}$ refers to the number of elements inside the brackets.)

4.2. Application of the proposed method to Rhodes

In order to apply this kind of approach to Rhodes, we introduce a rectangle enclosing the area between 26.9° and 28.6°E, and 35.4° and 36.85°N, as shown in Fig. 9. This rectangle plays the role of Ω in the previous section and contains parts of the regions 48, 29, 18, 19 and 20 of Fig. 7. Next, we produce, with the aid of a random point generator implemented by J. Burkardt (`http://people.sc.fsu.edu/~jburkardt/`), a number of points, say N, which are uniformly distributed in Ω and are marked with asterisks in Fig. 9. Finally, we extract their geographical coordinates which will play the role of the earthquake epicenters in the sequel.

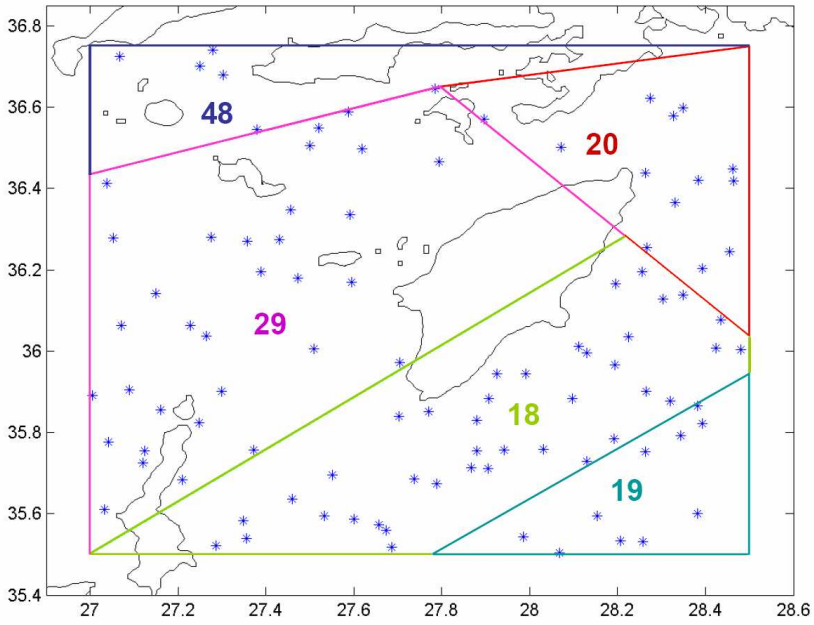

Figure 9: Rectangular area surrounding the island of Rhodes, the sub-areas with different source mechanism and the randomly selected epicenter locations. Boundaries between regions after Papazachos and Papazachou (1997).

As previously mentioned, the source parameters for each subregion in Fig. 7 have been inferred elsewhere (Papazachos and Papazachou, 1997; Moratto et al., 2007), at least to the extent possible given the existing earthquake population statistics. Specifically, the values of the Gutenberg-Richter parameters *b* and *a* are reported in Papazachos and Papazachou, 1997, p. 120, Table 7.1, while values of strike, dip and rake for each subregion, are taken from Moratto et al., 2007, their Table 1, and summarized in Table 3.

Region No.	Source name	b	a	Strike	Dip	Rake
18	Karpathos	0.96	4.53	184	47	262
19	Strabo	0.97	4.53	303	25	90
20	Marmaris	0.90	4.24	294	27	99
29	Rhodos	0.95	4.37	185	47	262
48	Cos	0.92	4.23	50	48	282

Table 3: Seismic source parameters for the areas surrounding Rhodes, see Fig. 7 for location.

The last main issue to be resolved is to assign to each of the subregions a value for the magnitude of the earthquake that reflects the seismicity of the region in a given time frame and, therefore, the potential tsunami hazard risk. Among the various quantities which have been proposed as measures of the seismicity of a specific region, we will use the

notion of the most probable maximum magnitude, which we now briefly present. According to the work of Epstein and Lomnitz (1966), concerning the occurrence of largest earthquake magnitudes over time, the largest annual earthquake magnitude is a random variable with cumulative distribution function (CDF) $G_Y(M) = \exp(-\alpha e^{-\beta M})$, $M \geq 0$. The parameters α, β are related to the parameters a, b, of the well-known empirical Gutenberg–Richter formula (*i.e.* $\log N = a - bM$, where N is the number of earthquakes in a given year with magnitudes M or larger) through the following relations

$$a = \frac{\ln \alpha}{\ln 10}, \quad b = \frac{\beta}{\ln 10}. \tag{1}$$

Then the probability of occurrence of an earthquake of magnitude M or greater in a time window t may be written as $[1 - \exp(-t\, 10^{a-bM})]$, where t is expressed in the same time unit as used for the computation of the constant a, *e.g.* one year; (Epstein and Lomnitz, 1966).

Denoting by $G_t(M) = \exp(-t\, 10^{a-bM})$ the corresponding CDF, the associated probability density function (PDF) is given by

$$g_{Y_t}(M) = b\, t\, (\ln 10)\, 10^{a-bM}\, \exp(-t\, 10^{a-bM}). \tag{2}$$

The *most probable maximum magnitude* ($\overline{M}$) is the modal value of the distribution, *i.e.* the value where the PDF (2) attains its maximum, and is given by the relation

$$\overline{M} = (a + \log t)/b. \tag{3}$$

(Intuitively, the most probable maximum magnitude may be viewed as the most frequently observed maximum annual magnitude in a window of duration t.)

	18	19	20	29	48
100 years	6.80	6.73	6.93	6.70	6.77
500 years	7.53	7.45	7.71	7.44	7.53
1000 years	7.84	7.76	8.04	7.76	7.86

Table 4: Most probable maximum magnitude ($\overline{M}$) for the areas surrounding Rhodes and for time windows of 100, 500 and 1000 years. $\overline{M}$ differs slightly for each region, according to the inferred a, b values.

We are now in a position to proceed with our simulations, assuming a magnitude equal to the most probable maximum magnitude in each region, which is easily computed from equation (3). The values of $\overline{M}$ for each region, and for time windows equal to 100, 500 and 1000 years are given in Table 4. Finally, for all simulations the depth is set at 7.5 km and the slip u is scaled to achieve the desired expected magnitude, using the relation $\overline{M} = [\log(\mu S\, u) + 16.01]/1.5$, where L is the length and W is the width of the fault, $S = L \cdot W$, and μ is the rigidity which is taken as 5×10^{11} dyn/cm^2. The dimensions of the fault are also scaled so that $W \approx L/2$.

Next, we have performed 100 runs with the MOST code for each time window (*i.e.* 100, 500 and 1000 years) using as epicenters the points depicted in Fig. 9, and as seismic input parameters the values reported in Tables 3 and 4.

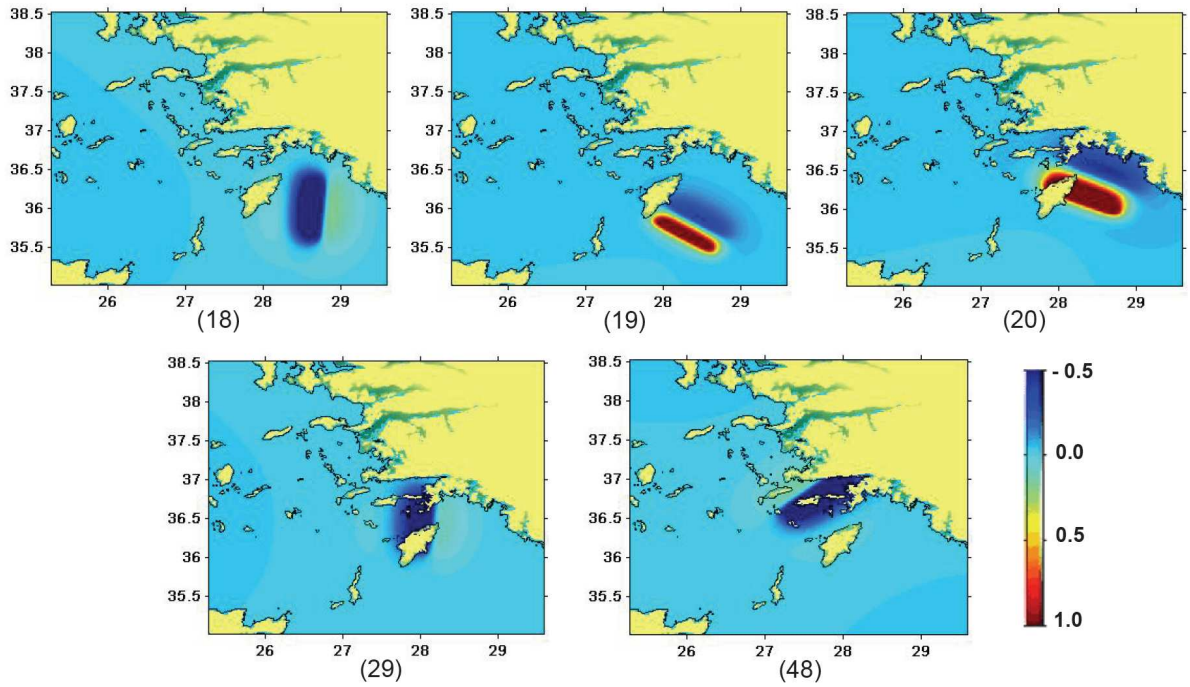

Figure 10: Typical initial conditions for each subregion. The numbers in the brackets refer to the different segment as shown in Fig. 9.

To provide a sense of the orientation of the initial conditions for epicenters lying in each subregion and corresponding to different source mechanisms, we show in Fig. 10 "typical" initial conditions. The region numbers in Fig. 10 correspond to those of Fig. 7 and Table 3.

We would like to note that, in order to check whether a $N = 100$ runs is adequate to provide reasonably stable estimates for the examined damage indicators, for the 500 years time window, we have experimented also with $N = 50$ and $N = 200$ random epicenters. A comparison of these results indicated that a value of $N = 50$ leads to relatively underestimated predictions compared to those obtained with $N = 100$, while there are no significant discrepancies in the estimates obtained with $N = 100$ and $N = 200$.

4.3. Discussion of Results

We now use the outcome of our simulations (one hundred simulations for each recurrence period of 100, 500, and 1000 years) to compute various inundation parameters of interest, and we present figures that summarize our results regarding the maximum inundation, maximum wave elevation and maximum flow depth.

The maximum inundation for a specific time window is estimated as follows: for each of the 100 simulations performed for that window, we calculate the inundation maximum over time, and then retain the largest of those 100 maxima. In Fig. 11, we superimpose the maximum inundation lines with colors red, yellow and purple, for time windows of 100, 500 and 1000 years, respectively, on an Ikonos multispectral image of the city of Rhodes. As

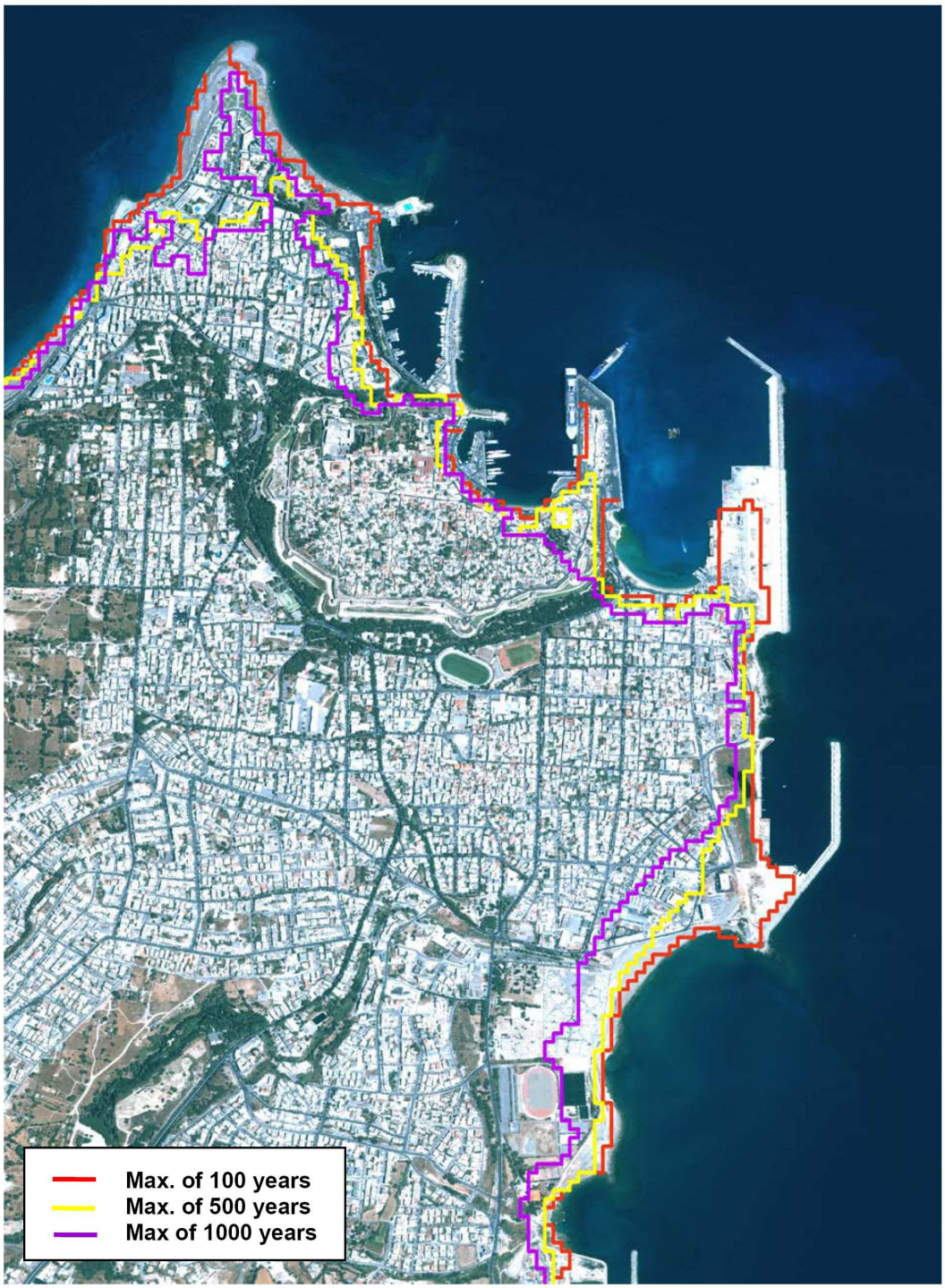

Figure 11: Probabilistic maximum inundation lines for 100, 500 and 1000 years superimposed on an Ikonos satellite image of the northern part of Rhodes.

expected, in all cases, most of the port and beach areas are flooded and the highest run-up values correspond to the 1000–year time window. Nevertheless, the 500–year probabilistic scenario also shows serious impact on the northern part of the city, while the 100–year scenario appears to affect a considerably narrower coastal area. In Fig. 12, we compare the maximum inundation line for 1000 years (purple line) versus the inundation line for the deterministic Scenario S4 (blue line), and notice that the probabilistic results seem to have a stronger impact on the city of Rhodes, while S4 (as well as S1–S3) exhibits, in general, higher run-up values in the eastern part of the coastal area under examination.

Figures 13, 14 and 15 present two-dimensional histograms for time windows of 100, 500 and 1000 years, respectively. The color palette corresponds to the frequency (*i.e.* number of times among the 100 runs for each time window) that a specific area is inundated; the blue color corresponds to a small frequency and the red color to a high frequency. For example, if we focus on Fig. 15, we see that, in terms of frequency of inundation, the beach on the north side of the city, the harbour, and the breakwaters, as well as most of the coastal area in the southeast of the city are all high risk areas. The frequency results shown in Figs. 13 and 14, for time windows of 100 and 500 years, respectively, follow the same trend, although with lower limits of inundation.

We have also computed the maximum elevation of the wave $\eta_{\max}(x, y)$ by taking the maximum, over 100 runs, of the largest wave elevations, and plot our results in Fig. 16. Additionally, we illustrate the elevation of the inundation line in separate horizontal and vertical subplots for the x and y coordinates, respectively, as shown in Fig. 16(a), 16(b) and 16(c), for time windows of 100, 500 and 1000 years. The results for the 100–year window, indicate that the elevation of the inundation line hardly exceeds 2 m around the harbour, while it essentially stays below 1.5 m for most of the eastern coastal area. The results for the 500–year window suggest that the elevation of the inundation line exceeds 5 m several times, and this is even more pronounced in the corresponding 1000-year results. Finally, comparing Figs. 5 and 16 underscores the conclusions from Fig. 12, *i.e.*, that the deterministic scenarios are more optimistic (*i.e.* lower impact) for the northern part of the city, and more pessimistic for the eastern part of the study area, compared to the results for 1000 years.

We have also calculated the parameter $h_{\max}(x, y)$ (the maximum flow depth) for all inland grid points. In Figs. 17(a), 17(b) and 17(c), we plot the maximum values of $h_{\max}(x, y)$ in meters for time windows of 100, 500, and 1000 years, respectively. Figure 17 confirms that the probabilistic analysis for the 100–year window does not imply a serious threat (since the highest flow depth value does not exceed 1 m), while for most of the coastal study area, $h_{\max}$ remains less than 0.4 m. On the contrary, in many locales, $h_{\max}$ is found to exceed 1 or 2 m, for the 500– and 1000–year time frames, respectively.

In Fig. 18, we show the frequency (*i.e.* how many times in 100 runs) the flow depth exceeded the threshold of 2 m, with blue corresponding to low values (rare exceedance), and red to high values (frequent exceedance). Our results indicate a low probability of exceeding a 2–m overland flow over a 100–year window, while the probability of exceedance reaches over 20% at many locales during the 1000–year window.

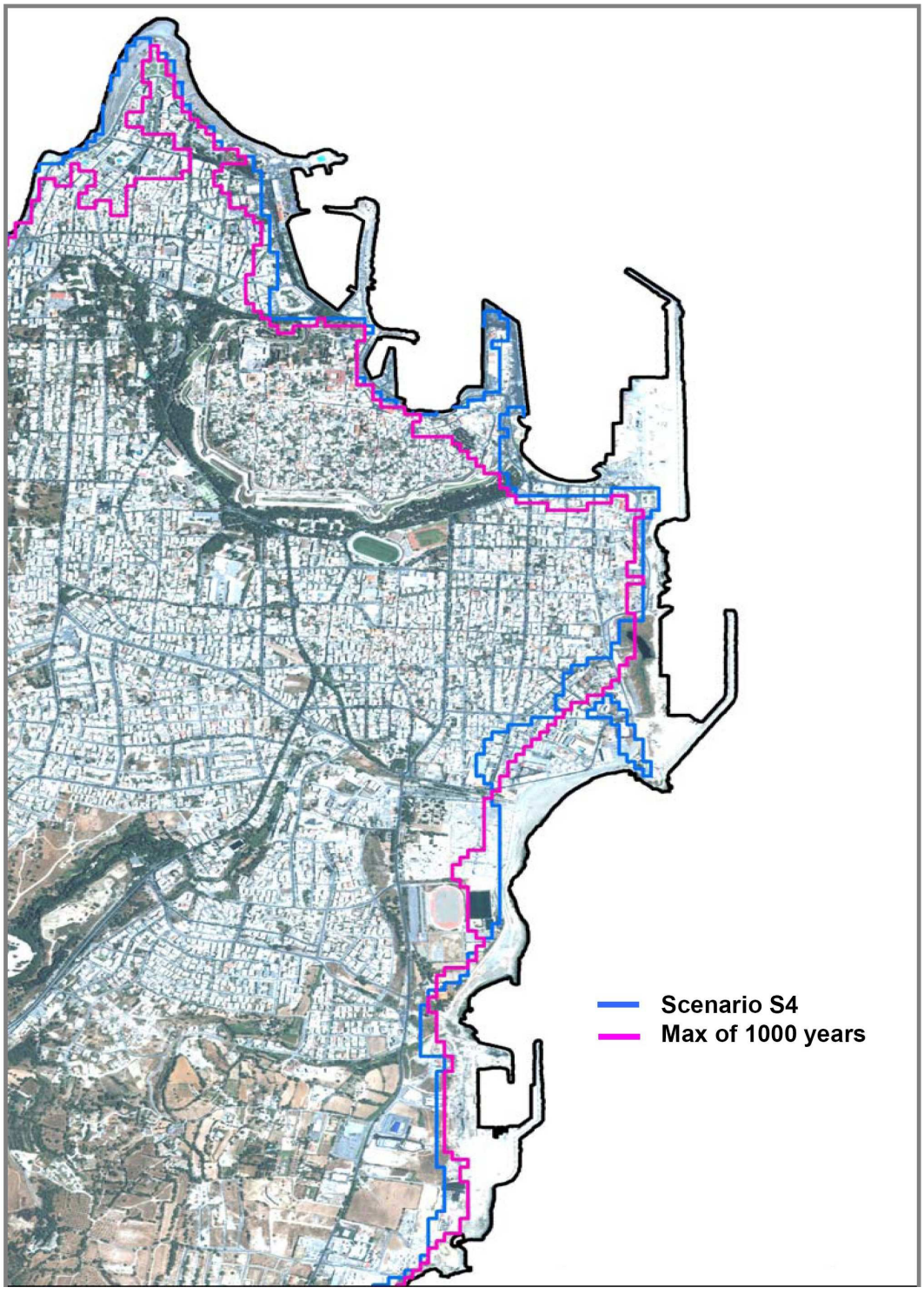

Figure 12: The probabilistic maximum inundation line for 1000 years versus the inundation line for the deterministic Scenario S4, superimposed on a satellite image of the city of Rhodes.

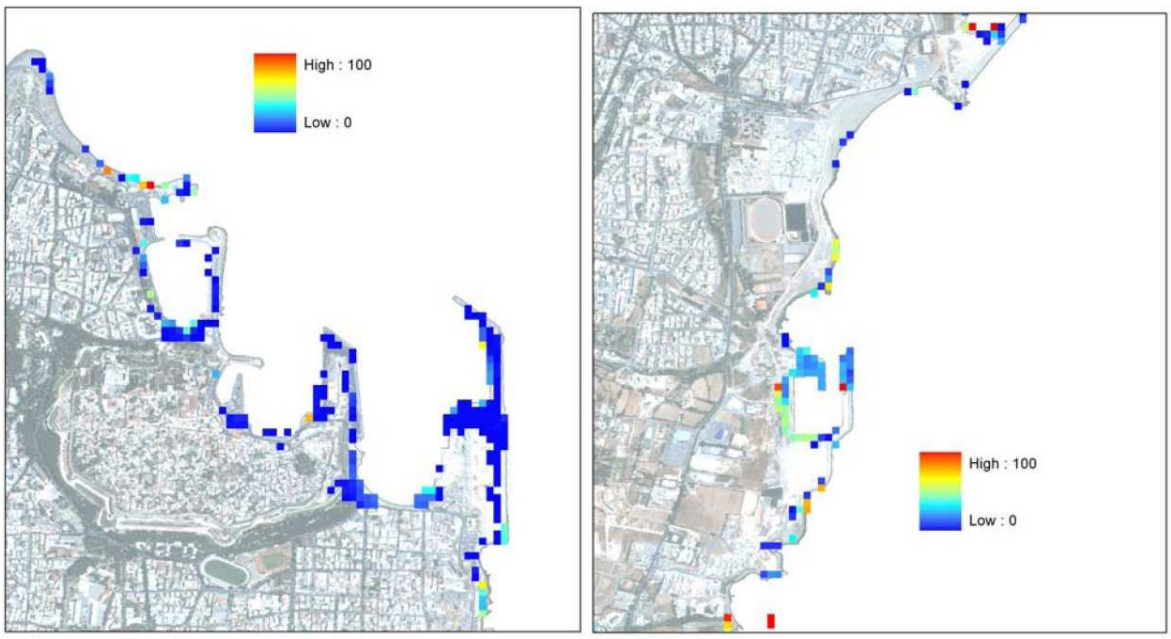

Figure 13: Probabilistic map showing the frequency of inundation among 100 runs for a time window of 100 years, for the main part of the city of Rhodes including the port (left), and for the Southeast coast only (right).

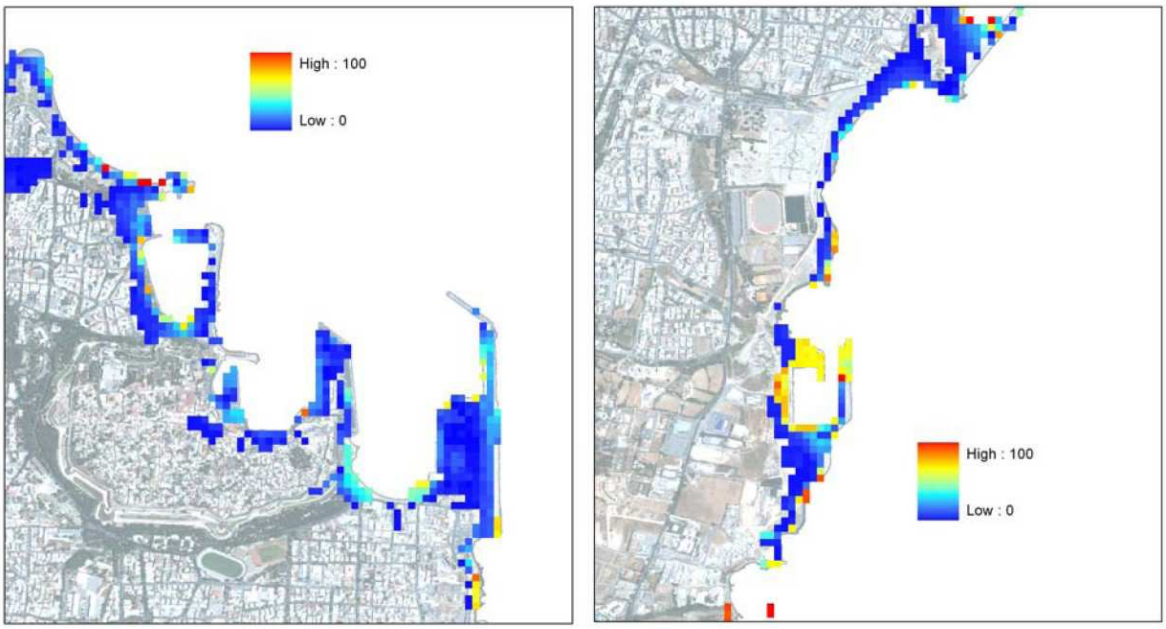

Figure 14: Probabilistic map showing the frequency of inundation among 100 runs for a time window of 500 years, for the main part of the city of Rhodes including the port (left), and for the Southeast coast only (right).

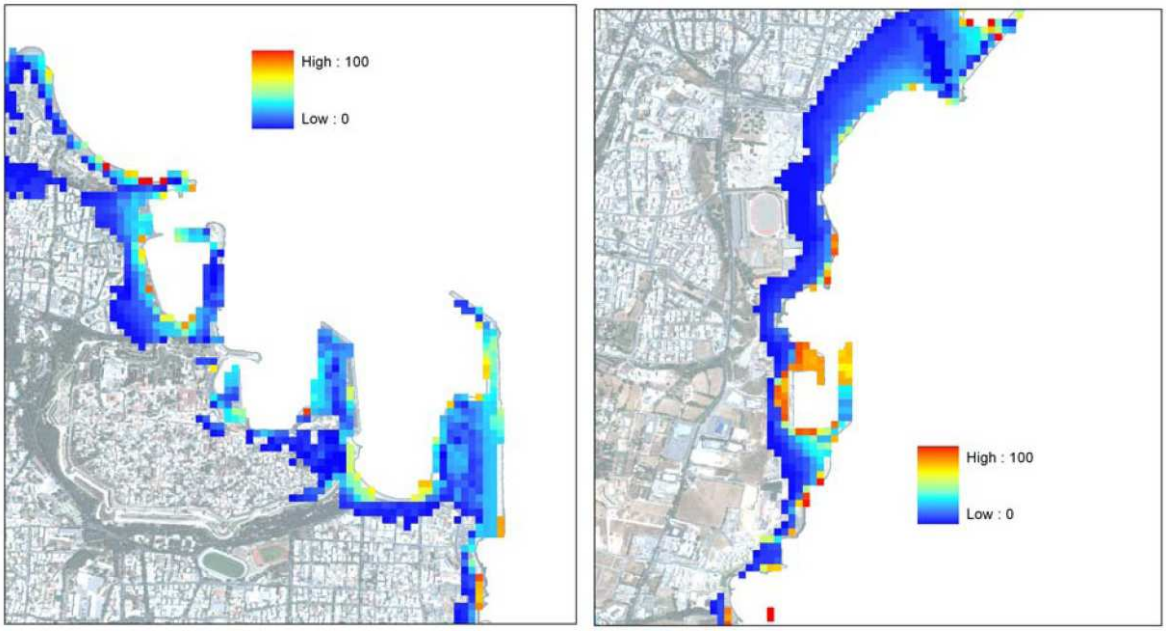

Figure 15: Probabilistic map showing the frequency of inundation among 100 runs for a time window of 1000 years, for the main part of the city of Rhodes including the port (left), and for the Southeast coast only (right).

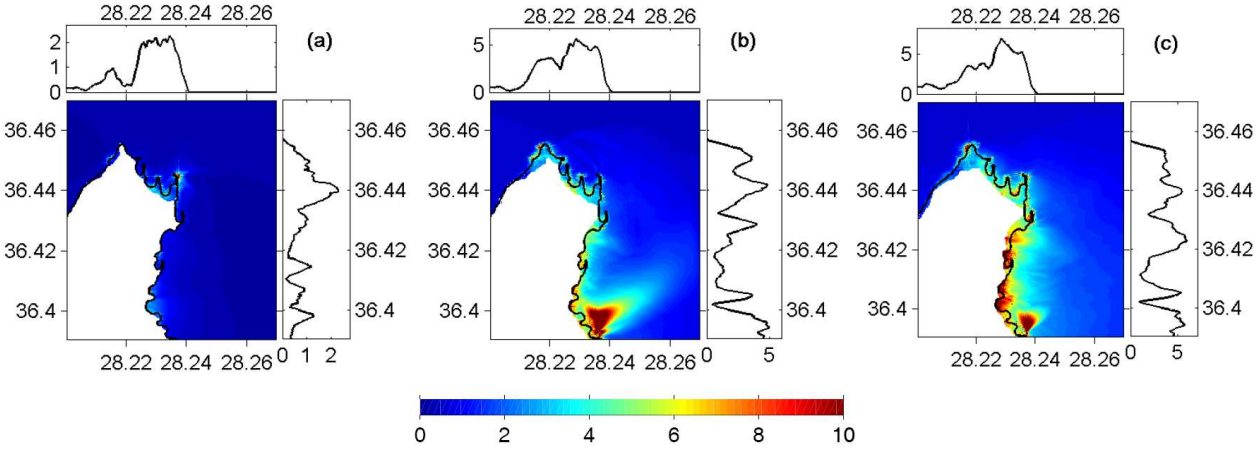

Figure 16: Maximum wave elevation η_{max} in meters and elevation of the inundation limits for time windows of 100 (a), 500 (b) and 1000 (c) years.

5. Conclusions

We have performed a systematic assessment of earthquake-generated tsunami hazards for the island of Rhodes using results from numerical simulations performed with MOST, coupled with accurate and updated bathymetry and topography data. We presented results of four hypothetical, credible, near-field 'worst' case scenarios, associated with seismic events of magnitude 8.0 to 8.4, and we have also produced results based on multiple tsunami scenarios,

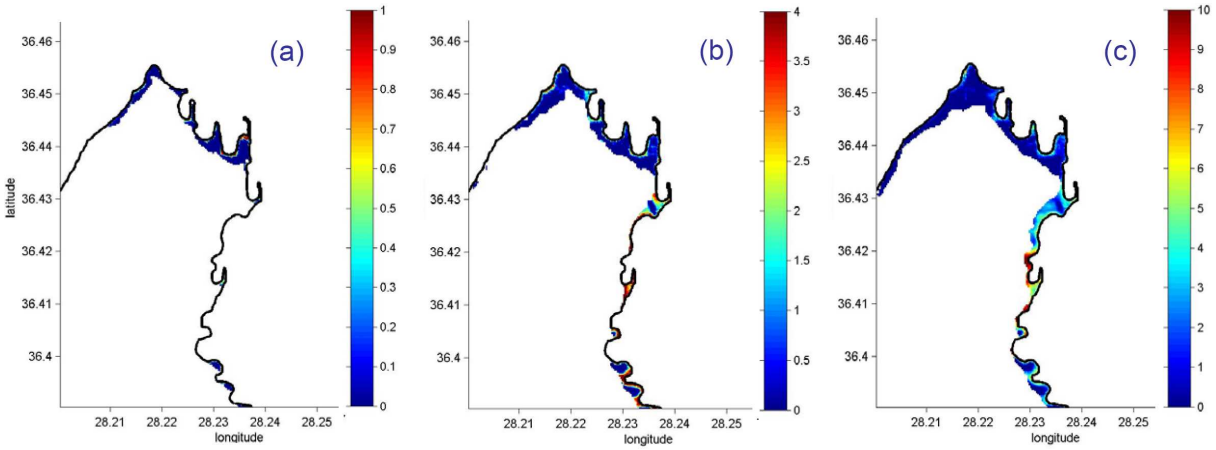

Figure 17: Results for the maximum flow depth (in meters) in 100 (a), 500 (b) and 1000 (c) years.

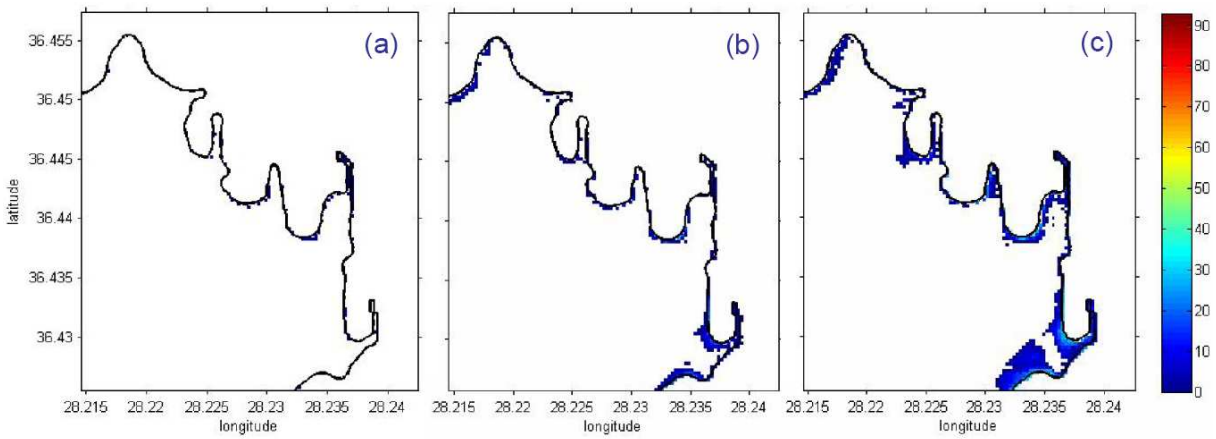

Figure 18: Frequency of exceedance (percent) of a 2m threshold value for the overland flow depth in time windows of 100 (a), 500 (b) and 1000 (c) years.

incorporating uncertainties stemming mainly from the location of the seismic source, for time windows of 100, 500 and 1000 years. A large total number of runs (100) has been used to obtain estimates of the examined hazard parameters (inundation, wave elevation and flow depth). Our results are not extracted by empirical relations, and they are illustrated in terms of lines superimposed on satellite images, in the form of maps indicating the estimated maximum values, or in terms of two-dimensional histograms reflecting the extent as well as the frequency of the corresponding hazard parameter.

Our results indicate that from the four deterministic scenarios examined, the most hazardous is S1. The impact of the latter is overall smaller than the 1000 years probabilistic results which incorporate hundreds of scenarios. Finally, we note that, the very short arrival times (< 20 min) for tsunami generated in the region of interest, suggest that

public education for self evacuation is imperative (Synolakis and Bernard, 2006). Ending, we note that post the 11 March 2011 Tohoku, Japan tsunami, it is important to reevaluate the seismic potential of the Hellenic Arc, and include earthquakes of size > 9.0, versus the size 8.0–8.4 included here. Absence of evidence for such megathrust events in the historic record may no longer be interpreted as evidence of absence.

Acknowledgements

This study was supported by the Sixth Framework Programme of EU project TRANSFER (Tsunami Risk ANd Strategies For the European Region) under contract no. 037058 to the Institute of Applied and Computational Mathematics of the Foundation for Research and Technology–Hellas (FORTH). We would like to express our thanks to Professors V. Dougalis, F. Dias and T. Miloh for their guidance, to Dr. M. Loulakis for fruitful discussions on the probabilistic approach, and to M. Diamandakis for his valuable help on GIS. Professors A. Yalciner and U. Kanoglu provided useful feedback.

References

Altınok, Y., Ersoy, Ş., 2000. Tsunamis observed on and near the Turkish coast. Nat. Hazards 21, 185–205.

Ambraseys, N.N., 1962. Data for the investigation of the seismic-waves in the Eastern Mediterranean. Bull. Seism. Soc. Am. 52, 895–913.

Ambraseys, N., 2009. Earthquakes in the Eastern Mediterranean and the Middle East: A Multidisciplinary Study of Seismicity up to 1900, Cambridge University Press.

Ambraseys, N., and Synolakis, C., 2010. Tsunami Catalogs for the Eastern Mediterranean, Revisited. Journal of Earthquake Engineering 14, 309–330.

Annaka, T., Satake, K., Sakakiyama, T., Yanagisawa, K., Shuto, N., 2007. Logic-tree approach for probabilistic tsunami hazard analysis and its applications to the Japanaese coasts. Pure Appl. Geophys. 164, 577–592.

Barberopoulou, A., Legg, M.R., Uslu, B., Synolakis, C.E., 2011. Reassessing the tsunami risk in major ports and harbors of California I: San Diego. Natural Hazards, 58(1), 479-496. DOI: 10.1007/s11069-010-9681-8.

Burbidge, D., Cummins, P. R., Mleczko, R., Thio, H. K., 2008. A probabilistic tsunami hazard assessment for Western Australia, Pure Appl. Geophys. 165, 2059–2088.

Chrysoulakis, N., Flouri, E., Diamandakis, E., Dougalis, V., Synolakis, C.E., Foteinis, S., 2008. Remote sensing in support of tsunami mitigation planning in the Mediterranean, in *Disaster Management & Emergency response in the Mediterranean Region*. Proceedings of the first EARSeL Conference 2008, M. Oluić (Ed.), 255–266.

Chrysoulakis, N., Abrams, M., Kamarianakis, Y. and StanisÅawski M., 2011. Validation of the ASTER GDEM for the area of Greece. Photogrammetric Engineering & Remote Sensing, 77, 157 – 165.

Courant, R., Friedrichs, K., Lewy, H., 1928. Über die partiellen Differenzengleichungen der mathematischen Physik. Math. Ann. 100, 32–74.

Dominey-Howes, D., 2002. Documentary and geological records of tsunamis in the Aegean Sea region of Greece and their potential value to risk assessment and disaster management. Nat. Hazards 25, 195–224.

Epstein, B., Lomnitz, C., 1966. A model for the occurrence of large earthquakes, Nature 211, 945–956.

Flouri, E.T., Kalligeris, N., Alexandrakis, G., Kampanis, N., and Synolakis, C.E., 2011. Application of a finite difference computational model to the simulation of earthquake generated tsunamis, *Applied Numerical Mathematics*, in press. DOI: 10.1016/j.apnum.2011.06.003.

Galanopoulos, A. G., 1960. Tsunamis observed in the coasts of Greece from antiquity to present time. Ann. Geofis. 13, 369–386.

Geist, E. L., Parsons, T., 2006. Probabilistic analysis of Tsunami hazards. Nat. Hazards 37, 277–314.

Geller, R.J., 1976. Scaling relationships for earthquake source parameters and magnitudes. Bull. Seism. Soc. Am. 66, 1501–1523.

González, F.I., Geist, E.L., Jaffe, B., Kânoğlu, U., Mofjeld, H., Synolakis, C.E., Titov, V.V., Arcas, D., Bellomo, D., Carlton, D., Horning, T., Johnson, J., Newman, J., Parsons, T., Peters, R., Peterson, C., Priest, G., Venturato, A., Weber, J., Wong, F., and Yalçıner, A., 2009. Probabilistic tsunami hazard assessment at Seaside, Oregon, for near- and far-field seismic sources. J. Geophys. Res. 114, C11023, doi:10.1029/2008JC005132.

Gusiakov, V.K., 1978. Static displacement on the surface of an elastic space. Ill-posed problems of mathematical physics and interpretation of geophysical data. Novosibirsk, VC SOAN SSSR, 23–51 (in Russian).

Kanamori, H., 1977. The energy release in great earthquakes. J. Geophys. Res. 82, 2981–2987.

Legg, M.R., Borrero, J.C., and Synolakis, C.E., 2004. Tsunami Hazards Associated with the Catalina Fault in Southern California, Earthquake Spectra vol. 20, n^o 3, 1–34, August 2004, Earthquake Engineering Research Institute.

Lipakis, M., Chrysoulakis, N., Kamarianakis, Y., 2008. Shoreline extraction using satellite imagery. In: E. Pranzini and E. Wetzel (eds): Beach Erosion Monitoring. Results from BEACHMED/e-OpTIMAL Project (Optimization des Techniques Integrees de Monitorage Appliquees aux Lottoraux) INTERREG IIIC South. Nuova Grafica Fiorentina, Florence, Italy, 81–95.

Liu, P. L.-F., Yeh, H., Synolakis, C. E. (Eds.), 2008. Advanced numerical models for simulating tsunami waves and run-up. Adv. Coastal Ocean Eng., vol. 10, World Scientific Publishing, Singapore.

Moratto, L., Orlecka-Sikora, B., Costa, G., Suhadolc, P., Papaioannou, Ch., Papazachos, C. B., 2007. A deterministic seismic hazard analysis for shallow earthquakes in Greece. Tectonophysics 442, 66–82.

Okada, Y., 1985. Surface deformation due to shear and tensile faults in a half space. Bull. Seism. Soc. Am., 75, 1135–1154.

Okal, E. A., Plafker, G., Synolakis, C. E., and Borrero, J. C., 2003. Near-Field Survey of the 1946 Aleutian Tsunami on Unimak and Sanak Islands. Bulletin of the Seismological Society of America 93, 1226-1234.

Okal, E.A., Synolakis, C.E., Uslu, B., Kalligeris, N., and Voukouvalas, E., 2009. The 1956 earthquake and tsunami in Amorgos, Greece. Geophys. J. Int. 178, 1533–1554.

Papadopoulos, G.A., Chalkis, B.J., 1984. Tsunamis observed in Greece and the surrounding area from antiquity up to the present times. Marine Geology 56, 309–317.

Papadopoulos, G.A., Daskalaki, E., Fokaefs, A., and Giraleas, N., 2007. Tsunami hazards in the Eastern Mediterranean: strong earthquakes and tsunamis in the East Hellenic Arc and Trench system. Nat. Hazards Earth Syst. Sci. 7, 57–64.

Papaioannou, Ch.A., Papazachos, B.C., 2000. Time-independent and time-dependent seismic hazard in Greece based on seismogenic sources. Bull. Seism. Soc. Am. 90, 22–33.

Papazachos, B.C., Coutitas, Ch., Hatzidimitriou, P.M., Karakostas, B.G., Papaioannou, Ch.A., 1986. Tsunami hazard in Greece and the surrounding area. Annales Geophysicae 4, 79–90.

Papazachos, B.C., Dimitriu, P.P., 1991. Tsunamis in and near Greece and their relation to the earthquake focal mechanisms. Nat. Hazards 4, 161–170.

Papazachos, B.C., 1996. Large seismic faults in the Hellenic Arc, Annali di Geofisica, vol. XXXIX, 891–903.

Papazachos, B.C., Papazachou, C., 1997. The earthquakes of Greece. Ziti Editions, Thessaloniki.

Power, W., Downes, G., Stirling, M., 2007. Estimation of tsunami hazard in New Zealand due to South American Earthquakes. Pure Appl. Geophys. 164, 547–564.

Shaw, B., Ambraseys, N.N., England, P.C., Floyd, M.A., Gorman, G.J., Higham, T.F.G., Jackson, J.A., Nocquet, J.-M., Pain, C.C., Piggott, M.D., 2008. Eastern Mediterranean tectonics and tsunami hazard inferred from the AD 365 earthquake. Nature Geoscience 1, 268–276.

Shiryaev, A.N., 1996. Probability. Springer.

Soloviev, S.L., 1990. Tsunamigenic zones in the Mediterranean Sea. Nat. Hazards 3, 183–202.

Spanos, P.D. and Zeldin, B.A., 1998. Monte Carlo treatment of random fields: a broad perspective. Applied Mechanics Review 51, 219–237.

Synolakis, C.E., and Bernard, E.N., 2006. Tsunami science before and after Boxing Day 2004. Philosophical Transactions A 364, 2231–2265.

Synolakis, C.E., Bernard, E.N., Titov, V.V., Kanoglu, U., and Gonzalez, F.I., 2008. Validation and Verification of Tsunami Numerical Models. Pure

and Applied Geophysics 165, 2197–2228.

Tadepalli, S., Synolakis, C.E., 1994. The Runup of N–waves. Proc. R. Soc. A, 445, 99–112.

Tinti, S., Armigliato, A., Pagnoni, G., and Zaniboni, F., 2005. Scenarios of giant tsunamis of tectonic origin in the Meditrranean. ISET Journal of Earthquake Technology, (Paper No. 464) 42, 171–188.

Titov, V.V., 1997. Numerical modeling of long wave run-up. Ph.D. thesis, University of Southern California, Los Angeles, California, 1997.

Titov, V.V., Synolakis, C.E., 1998. Numerical modeling of tidal wave run-up. J. Waterw. Port C.-ASCE, 124, 157–171.

Tselentis, G-A., Stavrakakis, G., Sokos, E., Ghika, F., and Serpetsidaki, A., 2010. Tsunami hazard assessment in the Ionian Sea due to potential tsunamigenic sources – results from numerical simulations. Nat. Hazards Earth Syst. Sci., 10, 1021–1030.

Uslu, B., 2008. Deterministic and Probabilistic tsunami studies in California from near and farfield sources. Ph.D. thesis, University of Southern California, Los Angeles, California.

Uslu, B., Borrero, J.C., Dengler, L.A., Synolakis, C.E., 2007. Tsunami inundation at Crescent City, California generated by earthquakes along the Cascadia Subduction Zone. Geophysical Research Letters, 34, L20601, DOI:10.1029/2007GL030188.

Yeh, H., Liu, P.L.-F., Synolakis, C.E. (Eds.), 1996. Long-wave run-up models. World Scientific Publishing, Singapore.